Bioactive Materials 6 (2021) 928–940

Contents lists available at ScienceDirect

Bioactive Materials

journal homepage: http://www.keaipublishing.com/biomat

Implantable PEKK/tantalum microparticles composite with improved surface performances for regulating cell behaviors, promoting bone formation and osseointegration

Xinglong Hu[a], Shiqi Mei[a], Fan Wang[a], Jun Qian[a], Dong Xie[b], Jun Zhao[c,***], Lili Yang[b,**], Zhaoying Wu[d], Jie Wei[a,*]

[a] Key Laboratory for Ultrafine Materials of Ministry of Education, East China University of Science and Technology, Shanghai, 200237, China
[b] Spine Center, Department of Orthopaedics, Shanghai Changzheng Hospital, Second Military Medical University, Shanghai, 200003, China
[c] Shanghai Key Laboratory of Stomatology, Shanghai Research Institute of Stomatology, Department of Orthodontics, Ninth People's Hospital Affiliated to Shanghai Jiao Tong University, School of Medicine, Shanghai, 200011, China
[d] School of Biomedical Engineering, Sun Yat-sen University, Guangzhou, Guangdong, 510006, China

ARTICLE INFO

Keywords:
Polyetherketoneketone
Tantalum
Composites
Surface performances
Osseointegration

ABSTRACT

Polyetherketoneketone (PEKK) exhibits admirable biocompatibility and mechanical performances but bioinert while tantalum (Ta) possesses excellent osteogenesis and osseointegration but high elastic modulus and density, and processing is too difficult and expensive. In the present study, combining of the advantages of both PEKK and Ta, implantable composites of PEKK/Ta were fabricated by blending PEKK with Ta microparticles of 20 v% (PT20) and 40 v% (PT40) content. In comparison with PT20 and PEKK, the surface hydrophilicity, surface energy, roughness and proteins adsorption as well as mechanical performances of PT40 significantly increased because of the higher Ta particles content in PEKK. Furthermore, PT40 exhibited the mechanical performances (e.g., compressive strength and modulus of elasticity) close to the cortical bone of human. Compared with PT20 and PEKK, PT40 with higher Ta content remarkably enhanced the responses (including adhesion, proliferation and osteogenic differentiation) of MC3T3-E1 cells *in vitro*. Moreover, PT40 markedly improved bone formation as well as osseointegration *in vivo*. In short, incorporation of Ta microparticles into PEKK created implantable composites with improved surface performances, which played key roles in stimulating cell responses/bone formation as well as promoting osseointegration. PT40 might have great potential for bear-loading bone substitute.

1. Introduction

Recent decades, tantalum (Ta) has been subjected to increasing interest as an implantable material for a variety of applications in orthopedics because of the excellent biocompatibility, corrosion resistance, and low bacterial adhesion as compared with those of stainless-steel and titanium (Ti) implants [1]. Currently, Ta is extensively applied as suture wires, cranioplasty plates and artificial joints as well as radiopaque markers, for surgical purposes [2]. Ta has historically been regarded as a bioinert material because of surface formation of a layer of passivating oxide with excellent chemical stability, which is highly unreactive and biocompatible in the body [3]. Early studies revealed that Ta had no obvious effect on osteoblast behaviors as compared with non-degradable plastics or metals *in vitro* cell culture, and thus did not stimulate inflammatory responses or induce giant cells in surrounding tissues *in vivo* animal experiments [4]. However, more recent investigations have demonstrated that Ta is not bioinert, which is an excellent substrate for stimulating the adhesion, proliferation and differentiation as well as mineralization of osteoblasts due to its high hydrophilicity, surface energy, high friction factor and nano or micron roughness, and so forth [5]. Nanostructured films of Ta not only promoted cell adhesion but also possessed outstanding antibacterial activity [6]. Moreover, porous Ta remarkably stimulated the proliferation and mineralization of osteoblasts as compared with cobalt chromium

Peer review under responsibility of KeAi Communications Co., Ltd.
* Corresponding author.
** Corresponding author.
*** Corresponding author.
E-mail addresses: yuzj_260@hotmail.com (J. Zhao), yangll@smmu.edu.cn (L. Yang), jiewei7860@sina.com (J. Wei).

https://doi.org/10.1016/j.bioactmat.2020.09.021
Received 6 August 2020; Received in revised form 23 September 2020; Accepted 23 September 2020

and Ti based biomaterials [7]. Furthermore, Ta allows bone tissues on on/in-growth and stimulates osteogenesis to achieve osseointegration, promoting the initial and long-term stability of implants [8]. It has been suggested that a natural thin layer of tantalum pentoxide existing on Ta surface might play a key role on its excellent biocompatibility, corrosion resistance, bioactivity as well as positive cell/tissue responses for bone on/in-growth [9]. Unfortunately, Ta is not as popular as Ti and its alloys in orthopedic implant manufactures, since the processing is too difficult and expensive [10]. Moreover, the significantly high elastic modulus and high density restricts the widespread acceptance of bulk Ta metal for implant applications [10].

As a class of high-performance polymer, polyaryletherketone (PAEK) has now gradually become the leading polymeric biomaterial in the fields of orthopedics and trauma, due to its admirable biocompatibility, mechanical strength, biostability, and radiolucency [11]. The representative PAEK materials mainly include polyetheretherketone (PEEK) and polyetherketoneketone (PEKK) as well as polyetherketoneetherketoneketone (PEKEKK) [12]. In the family of PAEK, PEEK has been extensively investigated and applied in trauma, neurosurgical and cranio-maxillofacial repair, spinal fusion, dental and joint substitutes [11,12]. As orthopedic and spinal implants for PAEK, concerns raised regarding the new bone formation and osseointegration, which has been one of the critical issues for long-term success rates of orthopedic implants [13]. Good osteointegration performance is necessary for a permanent orthopedic device, because the osteointegration will directly impact the initial and long-term stability of the implant [14].

PAEK is a non-degradable and bioinert polymer, therefore, the formation of fibrous tissue encapsulation around the PAEK implant and the weak osteointegration performance has been reported in previous studies [15]. The layer of fibrous tissues developed between bioinert implants and host bone tissue may be long-term unstable, which may eventually result in the loosening and failure of implants [16]. Many investigations have been carried to improve the bioactivity of PEEK for promoting bone formation and osteointegration, and these strategies include surface modification with either physical/chemical ways, and composites with bioactive fillers were applied [17,18]. However, these simple surface modification with physical/chemical methods might not be practical to produce implants because of the potential incompatibility with sterilization and cleaning procedures [17,18]. The blending of bioactive materials with PEEK is currently the preferred way to improve its bioactivity while maintaining the mechanical performances of the substrates [19]. Generally, bioactive PEEK based composites were produced by adding appropriate amount of bioactive materials such as bioactive glasses and tricalcium phosphate as well as hydroxyapatite into the PEEK matrix, which have been reported in previous investigations [20]. Zhu et al. [21] investigated Ta nanoparticles reinforced PEEK, which enhanced mechanical properties and promoted bone formation both *in vitro* and *in vivo*. Plasma immersion ion implantation (PIII) was applied to fabricate Ta-implanted PEEK (Ta ions were implanted energetically into PEEK), which stimulated responses of rat bone mesenchymal stem cells *in vitro* and improved osteointegration *in vivo* [22].

In recent years, PEKK, another representative PAEK material, has been increasingly investigated as a promising orthopedic biomaterial [23]. PEKK has been gradually applied as biomedical implants because it possesses better potential for spinal, orthopedic and dental applications than PEEK [23]. Compared with PEEK, PEKK has some advantages such as better mechanical performances, higher thermal stability and structural variation between semi-crystalline and amorphous phase as well as versatile chemistry because of two ketone bonds [23]. Furthermore, PEKK implantable materials have received acceptance by medical implant manufacturers who had gained permit from the U.S. Food and Drug Administration [24].

In the present study, by combination of the advantages of both PEKK and Ta, PEKK/Ta composites were fabricated by blending PEKK with Ta microparticles of 20 v% (PT20) and 40 v% (PT40) content. The purpose of this study was to design an implantable composite with excellent bioactivity and mechanical performances (e.g., compressive strength, elastic modulus) close to the cortical bone of human, which could be used for bear-loading bone substitute. We assume that blending of Ta microparticles with PEKK could improve the mechanical performances as well as surface performances (including surface hydrophilicity, surface energy, roughness and protein adsorption) of the composites, which could stimulate the cells responses (e.g., adhesion, proliferation, alkaline phosphatase activity and osteogenesis gene expressions) *in vitro*, and promote bone formation and osseointegration *in vivo*.

2. Materials and methods

2.1. Preparation of specimens

The PEKK/Ta composites containing Ta content of 20 v% (PT20) and 40 v% (PT40) were prepared by cold-pressing and sintering method. The PEKK powders were purchased from OXPEKK-C, Oxford Performance Materials, America. In addition, the Ta powders were purchased from Grandview Materials Inc., America. Specifically, 1.9 g PEKK powders and 8.1 g tantalum powders (20 v% Ta), or 1.44 g PEKK powders and 18.56 g tantalum powders (40 v% Ta) were dispersed into 500 mL deionized (DI) water with ultrasonic stirring for 3 h. According to our pre-experiment, when the Ta content further increased (more than 40 v%), the aggregation of Ta microparticles became obvious in the PEKK matrix, and the mechanical properties of the composite decreased. Therefore, we chose 40 v% Ta content as the highest ratio in the PEKK.

After the dispersions of PEKK/Ta mixtures were centrifuged at 1000 rpm (low velocity) for 5 min (short time) to remove the water, the mixtures were collected and dried at 50 °C in a draught drying cabinet (DHG-9070A, Bluepard, Shanghai, China) for 24 h to obtain two kinds of preliminary mixed powders (PT20 and PT40). Afterwards, the mixed powders were further treated in a high-speed ball mill (QM-3B, Nanjing T-Bota Scietech Instruments & Equipment Co., Nanjing, China) at a mixing speed of 600 rpm for 24 h, and the mixtures were further dried at 50 °C for 24 h. Processing parameters (centrifugal speed and time, and milling speed and time) had obvious effects on the distribution of Ta particles within PEKK bulk material. Therefore, the parameters were optimized to prepare the PEEK/Ta composites.

The as-prepared mixture powders were placed into the stainless-steel molds (Φ12 × 2 mm, Φ12 × 20 mm and Φ4 × 5 mm) and compressed by compressing machine (YP-40T, Jinfulun Technology Co., China) under the pressure of 4 MPa. Three types of specimens with different sizes were prepared, in which the specimens (Φ12 × 2 mm, Φ12 × 20 mm) were utilized for *in vitro* tests and specimens (Φ4 × 5 mm) were used for *in vivo* tests. The as-prepared specimens were sintered in muffle furnace at 355 °C for 6 h. Afterwards, the specimens were polished with abrasive papers (2000 grit), and ultrasonically washed with ethanol and DI water for 3 times, respectively, which were then dried at 60 °C for 12 h to obtain PT20 and PT40. Moreover, the same sizes of PEKK samples without Ta were prepared by the same method used as controls.

2.2. Characterization of specimens

The particle size of Ta was characterized by field-emission scanning electron microscopy (SEM, S-4800, Hitachi, Japan) and dynamic light scattering (DLS, Zetasizer SZ100, Horiba, Japan). Specifically, due to the dust sensitivity of DLS measurements, the DLS tubes were separately washed with pure water and acetone for 2 times. After dried in the oven overnight, the tubes were wrapped by using aluminum foil, and further cleansed with distilled acetone through an acetone fountain setup. The 1 g Ta powders were dispersed into 50 mL DI water with

constant mechanical stirring for 2 h and ultrasonic stirring for 2 h, respectively. After that, a disposable syringe was used to draw 2.5 mL of the dispersion into the tube. Then, DLS was applied to measure the particle size of Ta in the dispersion at 25 ˚C. Measurement conditions are as follows: water refractive index (RI) of 1.3328, with a viscosity of 0.8878 cP. All the measures were performed in triplicates.

The composition, phase structure and surface morphology of the as-prepared specimens (PEKK, PT20, PT40) were determined by Fourier transform infrared spectrometry (FTIR, Nicolet 6700, Nicolet, USA), rotating anode X-ray powder diffractometer (XRD, D/MAX 2550 VB/PC, Rigaku Co., Japan), and field-emission scanning electron microscopy (SEM, S-4800, Hitachi, Japan), respectively. The surface morphology and roughness (Ra, arithmetical mean deviation of the profile) of the specimens were determined by laser confocal 3D microscope (VK-X 110, Keyence Co., Japan). The elemental composition and distribution of the specimens were characterized by energy dispersive spectrometry (EDS, S-4800, Hitachi, Japan).

The compressive strength of the specimens (Φ12 × 20 mm) was measured by using a mechanical testing machine (E44.304, MTS Co., China) according to the GB/T1041-2008 Standard. The specimens were loaded with the pressure of 30 kN load at a speed of 2 mm/min until the specimens were crushed. The computer automatically plotted the stress–strain curve. The compressive strength was recorded as the peak of the stress-strain curve of the elastic deformation stage, and the elastic modulus is calculated as the slope of the linear part (elastic deformation stage) in the stress–strain curve. The three-point bending tests were performed to determine the bending strength of the specimens according to the GB/T 9341-2008 Standard with the loading rate of 2 mm/min. The span was 64 mm and head of loading device was composed of steel cylinders 10 mm in diameter. The water contact angle and diiodomethane contact angle of the specimens were characterized by contact angle measurement (CAM, JC2000D1, Shanghai zhongchen digital technique apparatus Co., China). The surface energy of the specimens was calculated according to the Owens two-liquid method [25].

2.3. Protein adsorption

The adsorption of proteins was determined by bicinchoninic acid protein assay kit (BCA, Pierce Biotechnology Inc., USA) via utilizing standard procedure according to the manufacturer's instructions. The specimens were placed into 24-well plates, then the protein solutions (5 mg/mL Bovine Serum Albumin (BSA), 30 μg/mL fibronectin (Fn)) were added into plates. After incubated at 37 ˚C for 4 h, the specimens were taken out, and then washed with PBS (3 times) to remove the loosely adsorbed proteins. The specimens were exposed to 5% sodium dodecyl sulfate (SDS) under shaking at 37 ˚C to release the adsorbed proteins. The solutions were collected, and then the amounts of proteins were determined utilizing the BCA assay kit.

2.4. Cells responses in vitro

Mouse osteoblast-like MC3T3-E1 cells (American Type Culture Collection, Chinese Academy of Sciences, China) were cultured in Minimum Essential Medium (α-MEM, Gibco BRL, Thermo Fisher Scientific, USA) supplemented with 10% fetal bovine serum (FBS, Gibco, Thermo Fisher Scientific, USA), 100 U/mL penicillin and 100 μg/mL streptomycin sulfate (Gibco BRL, Thermo Fisher Scientific, USA) in a humidified atmosphere of 5% CO_2 at 37 ˚C. Before cell culture, the specimens of PEKK, PT20 and PT40 were sterilized by ethylene oxide, which was placed in 24-well plates. The cells were cultured on the specimens at a density of 5×10^4 cells per well for determining the attachment, proliferation and osteogenic differentiation of the cells. The medium was renewed every 2 days.

2.4.1. Cell morphology and adhesion

To observe the morphology of MC3T3-E1 cells cultured with PT composites, the cells were seeded on specimens and allowed to attach for 1 and 3 days. At the time points, the medium was removed, and the cells/specimens were rinsed three times with PBS and fixed with 2.5% glutaraldehyde solution for 1 h. The fixed cells were washed with PBS for 3 times, and fluorescein isothiocyanate-Phalloidin (FITC-Phalloidin, Yeasen Biotech, China) was added on the specimens to stain F-Actin for 40 min, then the FITC-Phalloidin solution was removed, and 2-(4-Amidinophenyl)-6-indolecarbamidine dihydrochloride (DAPI, Beyotime Biotech, China) was added to stain nuclei of MC3T3-E1 cells for 5 min. The stained cells on specimens were observed by confocal laser scanning microscopy (CLSM, Nikon A1R, Nikon Co., Japan). The morphology of the cells on the specimens was also observed by SEM after dehydrated in graded ethanol solutions (10, 30, 50, 70, 85, 90, 95 and 100 v/v%) for 10 min and drying at 25 ˚C. The adhesion ratio of the cells on the specimens for different time was assessed by measuring optical density values, which were determined at 450 nm by utilizing a microplate reader (Synergy HTX, Bio-Tek, USA) with 620 nm as the reference wavelength.

2.4.2. Cell proliferation and alkaline phosphatase (ALP) activity

After 1, 3 and 7 days of incubation, the cell proliferation assay was performed using CCK-8 (Cell Counting Kit-8, Dojindo Molecular Technologies Inc., Japan) according to the manual instructions. Briefly, at each time point, the specimens were gently rinsed for 3 times with PBS to remove the unattached cells and transferred to a new 24-well plate, then 500 μL α-MEM containing 50 μL CCK-8 solution was added to each well. After incubating for 4 h, 100 μL supernatant from each well was transferred into a 96-well plate and the optical density (OD) at 450 nm was measured using a microplate reader (Synergy HTX, Bio-Tek, USA) with 620 nm as the reference wavelength.

At specific culturing times (7, 10 and 14 days) of MC3T3-E1 cells on the specimens, the medium was aspirated, and the specimens were gently rinsed with PBS three times, followed by lysis with 1% Nonidet P-40 solution. Then the cell lysate was obtained and centrifuged. The supernatant was incubated with 2 mg/mL *p*-nitrophenyl-phosphate (pNPP, Sangon, China) solution supplemented with 0.1 mol/L glycine and 1 mmol/L $MgCl_2{\cdot}6H_2O$ solution for 30 min at 37 ˚C. The reaction was quenched with 0.1 mol/L NaOH solution. The absorbance of ALP was measured using a Microplate Reader (SPECTRAmax 384, Molecular Devices, USA) at the wavelength of 405 nm. A bicinchoninic acid protein assay (BCA, Pierce Biotechnology Inc., USA) kit was utilized to determine the total protein quantity for normalization. The ALP activity was expressed as absorbance at 405 nm divided by the total protein quantity.

2.4.3. Osteogenesis related genes expressions

The expressions of osteogenic genes were determined by real-time PCR. For detecting osteogenic related gene expression, after cells were cultured on specimens (density of 10^5 cells per well) at 3, 7 and 14 days after culturing, total RNA was isolated from MC3T3-E1 cells using Trizol reagent (Invitrogen, USA) according to the manufacturer's instructions. Afterwards, 1 μg of total RNA was reversely transcribed into complementary DNA (cDNA) using PrimeScript First Strand cDNA Synthesis Kit (TaKaRa, Japan). Real-time PCR analysis was performed with Bio-Rad real-time PCR system (Bio-Rad, USA) on markers of runt-related transcription factor 2 (Runx2), ALP, osteopontin (OPN), osteocalcin (OCN) with glyceraldehyde-3-phosphate dehydrogenase (GAPDH) as the house-keeping gene for normalization. The forward and reverse primer sequences for the selected genes were listed in Table 2.

Table 1
Mechanical properties of PT composites.

Specimens	Compressive Strength (MPa)	Bending Strength (MPa)	Elastic modulus (GPa) <
PEKK	134.96 ± 8.76	162.30 ± 9.76	3.71 ± 0.26
PT20	169.47 ± 11.59	198.91 ± 12.25	5.20 ± 0.31
PT40	192.77 ± 12.98	220.40 ± 13.34	7.34 ± 0.53
Human cortical bone [26,27]	174.00 ± 35.00	177.88 ± 23.80	3.73 ± 1.27

2.5. Bone formation and osseointegration in vivo

2.5.1. Surgical procedure

All the *in vivo* procedures were carried out with the approval of the Animal Care and Experiment Committee of Shanghai Ninth People's Hospital affiliated to Shanghai Jiao Tong University (Shanghai, China). Eighteen male beagle dogs (weight: 9–15 kg, age: 18 months) were used to conduct the femur implantations, which were divided into three groups as follows corresponding to PEKK, PT20, PT40. All surgical operation was conducted under sterile conditions. After general anesthesia with intraperitoneal injection of pentobarbital sodium (40 mg/kg, Sigma–Aldrich, USA), the surgical site was sterilized with iodophor disinfectant. Then two holes (4.0 mm in diameter; 5.0 mm in depth) were created with a hand drill on the bilateral epicondyle of femurs, and the implants (PEKK, PT20, PT40) were pressed into the holes.

For each group at 4 and 12 weeks after operation, the dogs were euthanatized by intraperitoneal injection of overdosed pentobarbital sodium, and the femurs containing implants were fixed in 4% phosphate-buffered formalin solution.

2.5.2. Micro computed tomography (Micro-CT) evaluation

High-resolution images of the new bone around the implants were obtained by Micro-CT (Skyscan 1172, Bruker, USA). The parameters of scanning were set at 80 kV (X-ray source voltage), 200 μA (beam current) and 900 msec (exposure time) with a resolution of 15 μm. A polygonal region of interest (ROI) in 100 slices with approximate 1 mm wide ring around the implant was chosen, which represented the newly formed bone. The three-dimensional (3D) images were reconstructed from the volume of interest, where an optimized threshold was used to isolate the bone and materials from the background using NRecon (Skyscan, USA) and CTvol program (Skyscan, USA). The bone mineral density (BMD), bone volume/total volume (BV/TV), trabecular number (Tb.N) and trabecular thickness (Tb.Th) were determined by CTAn program (Skyscan, USA).

2.5.3. Histological and Bone-Implant Contact analysis

After being measured by Micro-CT, the femurs were dehydrated by ascending concentrations of ethanol (70, 80, 85, 90, 95 and 100 v/v%), and then embedded in polymethyl methacrylate. The specimens were cut into sections (thickness of 150 μm) perpendicular to the long axis of implants using a Leica SP1600 saw microtome (Leica, Germany), and then polished (thickness of 50 μm). Afterwards, the sections were stained by uing Van Gieson's picro fuchsin staining (VG) to visualize the mineralized bone tissue (red). The images were captured with a microscope (Leica DM4000B, Germany) for histological examination, and the index of Bone-Implant Contact (BIC) was analyzed with Image-Pro Plus 6.0 (Media Cybernetics, USA).

2.5.4. Push-out test

The biomechanical bonding strength of bone-implant interfaces was measured by push out test using the universal material testing system (Instron, USA). A custom designed holder was used to fix the testing specimens to ensure that the test stress is along the long axis of implants. A special designed crosshead with the same diameter as PT implants was prepared, which could be used to apply load on implants. Push out test was conducted at a loading rate of 5 mm/min with applied stress ranging from 0 to 600 N. Three samples in each group were measured under the same condition. During the pushing period, the stress-strain curve was recorded, and the failure load was determined as the peak load value of the stress-strain curve.

2.6. Statistical analysis

Statistical analysis was assessed using one-way analysis of variance (ANOVA). Quantitative data were expressed as the mean ± standard deviation (SD) of the results of at least three independent experiments. The differences were considered statistically significant at $^{*}p < 0.05$, $^{**}p < 0.01$, and $^{\#}p < 0.05$.

3. Results

3.1. SEM, FTIR and XRD analysis of specimens

Fig. 1a reveals the SEM image of morphology of Ta particles. The Ta particles with the size of around 1 μm exhibited irregular shape. Fig. 1b reveals the DLS of size distribution of Ta particles. The size distribution of Ta particles was ranged from 0.4 μm to 2.5 μm, and most of Ta particles were ~1 μm.

Fig. 1c is the FTIR spectra of PEKK, PT20, PT40 and Ta. The spectra of both PT20 and PT40 reveal the same characteristic peaks as PEKK. The peaks at 1650, 1490 and 920 cm^{-1} corresponded to the diphenyl ketone group, and the peak at 1586 cm^{-1} was attributed to C=C stretching vibrations in the aromatic ring. Bands at 1232 and 1154 cm^{-1} were related to asymmetric stretching vibration of C−O−C bond in the diaryl groups. No obvious characteristic peaks appeared in Ta. The characteristic peaks of PEKK were found in both PT20 and PT40.

The XRD patterns of PEKK, PT20, PT40 and Ta are showed in Fig. 1d. The peaks of $2\theta = 38.5^{\circ}$, 55.6° and 69.7° could be observed in PT20, PT40 and Ta, which were assigned to the characteristic peaks of Ta. Moreover, the peaks of $2\theta = 15.5^{\circ}$, 18.5°, 22.6°, and 28.7° in PEKK, PT20 and PT40 were belonged to the characteristic peaks of PEKK. In both PT20 and PT40, the characteristic peaks of Ta exhibited high crystalline phase while the characteristic peaks of PEKK revealed low crystalline phase.

3.2. Surface morphology, roughness, composition and mechanical properties

Fig. 2(a–f) reveals the SEM micrographs of PEKK, PT20 and PT40.

Table 2
Primers used for RT-PCR.

Gene	Forward primer sequence (5′–3′)	Reverse primer sequence (5′–3′)
Runx2	AACAGCAGCAGCAGCAGCAG	GCACGGAGCACAGGAAGTTGG
ALP	TGACCGTCCTGCTGGAACTCG	CCACTGCCACACTTGTCACAGAG
OPN	GACGATGATGACGACGACGATGAC	GTGTGCTGGCAGTGAAGGACTC
OCN	AGACCTAGCAGACACCATGAGGAC	TGAGGTAGCGCCGGAGTCTATTC
GAPDH	ACAGCAACAGGGTGGTGGAC	TTTGAGGGTGCAGCGAACTT

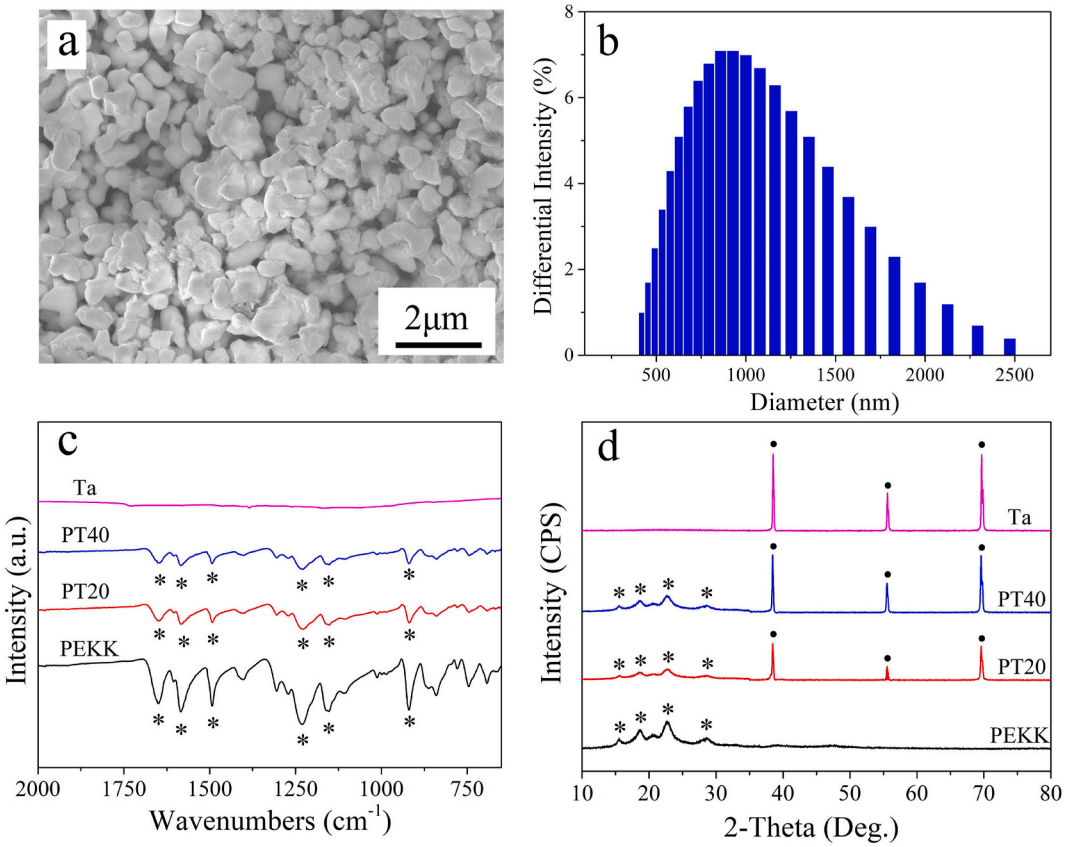

Fig. 1. SEM image (a) and DLS of size distribution (b) of Ta particles, and FTIR spectra (c) and XRD patterns (d) of PEKK, PT20, PT40 and Ta; * represents the characteristic peaks of PEKK, ●represents the characteristic peaks of Ta.

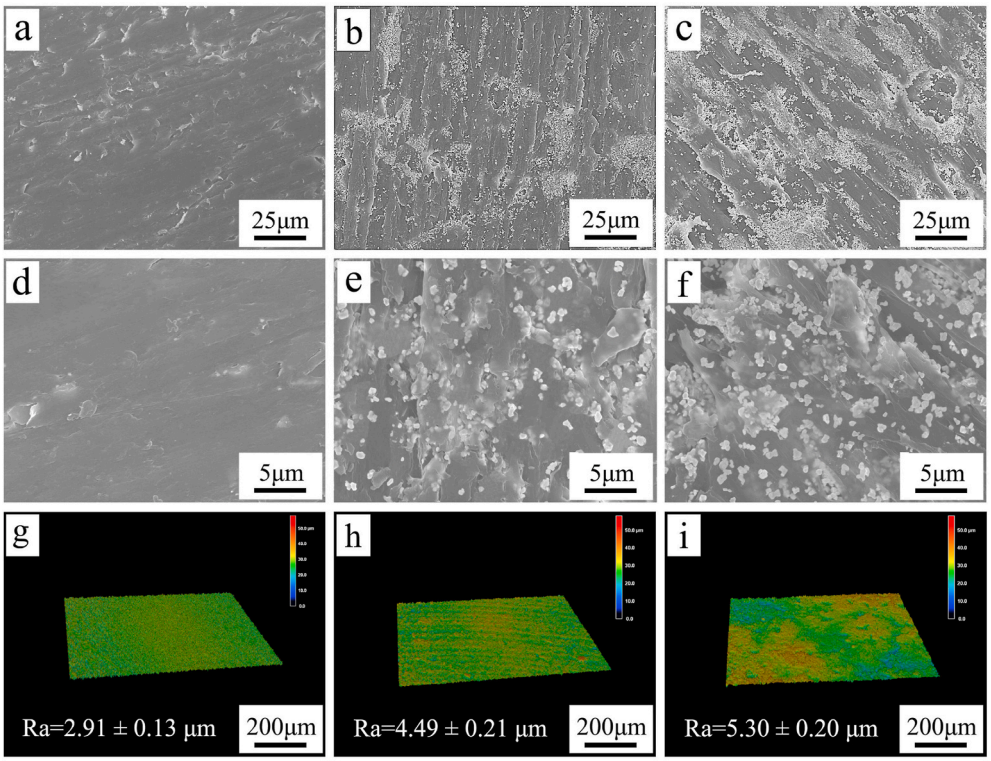

Fig. 2. SEM micrographs of surface morphology of PEKK (a, d), PT20 (b, e), PT40 (c, f) under different magnification, and laser microscope 3D images and roughness of PEKK (g), PT20 (h) and PT40 (i).

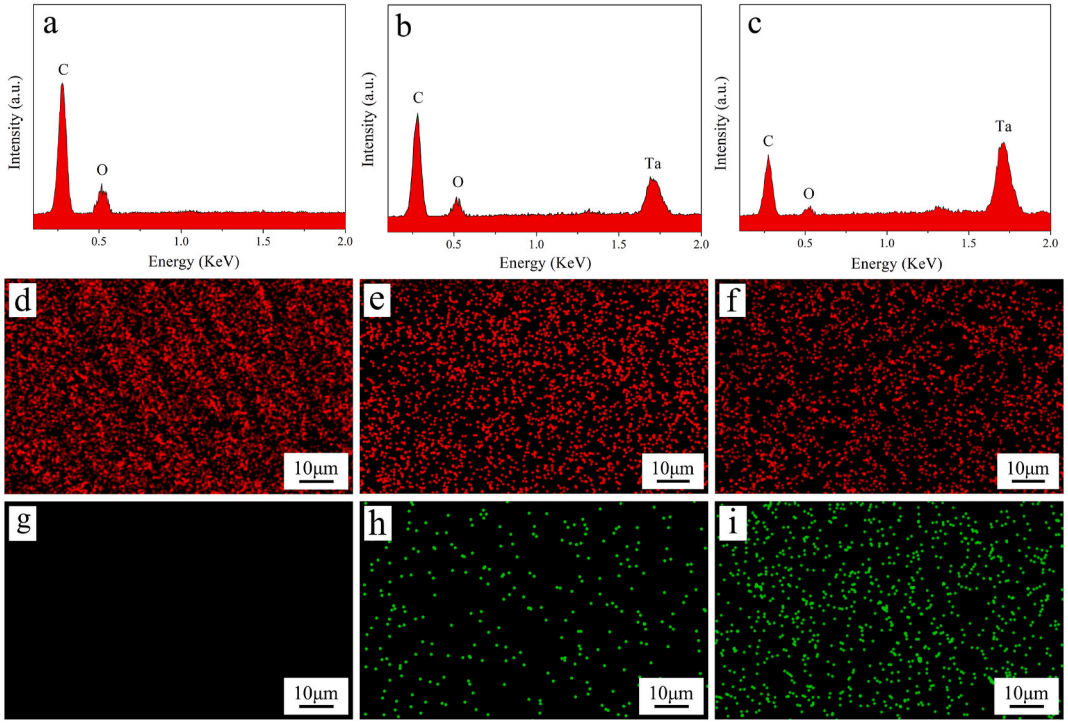

Fig. 3. EDS spectrum of PEKK (a), PT20 (b) and PT40 (c), and EDS mapping of PEKK (d, g), PT20 (e, h) and PT40 (f, i), in which the element distribution of carbon in red (d, e, f) and Ta in green (g, h, i). (For interpretation of the references to colour in this figure legend, the reader is referred to the Web version of this article.)

PEKK showed a smooth surface while PT20 and PT40 exhibited rough surfaces. Moreover, Ta particles were found to disperse on the surface of the composites, and more Ta particles were found on PT40 than PT20.

Fig. 2(g–i) shows the laser microscope 3D images and roughness of PEKK, PT20 and PT40. PEKK exhibited a smooth surface while the composites revealed rough surface. The roughness of PEKK, PT20 and PT40 were 2.91 ± 0.13 μm, 4.49 ± 0.21 μm, 5.30 ± 0.20 μm, respectively.

Fig. 3a, b, c reveals the EDS spectrum of PEKK, PT20 and PT40. The intensity of carbon (C) and oxygen (O) peaks gradually decreased with the increase of Ta content, while the intensity of Ta peak increased. Fig. 3(d–i) reveals the EDS mapping of PEKK, PT20 and PT40. The signal dots of both C (red dots) and Ta (green dots) elements were found to disperse on the surface of specimens. The content of C element gradually decreased with the increase of Ta content, while the content of Ta element increased accordingly.

Table 1 shows the mechanical properties (Compressive strength, Bending Strength and Elastic modulus) of PEKK, PT20 and PT40 and human cortical bone. The compressive strengths of PEKK, PT20, PT40 and human cortical bone were 134.96 ± 8.76 MPa, 169.47 ± 11.59 MPa, 192.77 ± 12.98 MPa and 174.00 ± 35.00 MPa, respectively. Bending Strength of PEKK, PT20, PT40 and human cortical bone were 162.30 ± 9.76 MPa, 198.91 ± 12.25 MPa, 220.40 ± 13.34 MPa and 177.88 ± 23.80 MPa, respectively. Elastic modulus of PEKK, PT20, PT40 and human cortical bone were 3.71 ± 0.26 GPa, 5.20 ± 0.31 GPa, 7.34 ± 0.53 GPa and 3.73 ± 1.27 GPa, respectively.

3.3. Hydrophilicity, surface energy and protein adsorption

The hydrophilicity of the specimens was assessed by testing the water contact angle, and the surface energy of the specimens could be calculated with water contact angle and diiodomethane contact angle. The water and diiodomethane contact angles of the specimens are shown in Fig. 4 (a, b). The water contact angle of PEKK, PT20 and PT40 were 82.00 ± 0.50°, 77.00 ± 0.50° and 57.00 ± 0.50°. The diiodomethane contact angle of PEKK, PT20 and PT40 were 58.00 ± 0.5°, 25.50 ± 0.50° and 23.50 ± 0.50°, respectively.

The surface energy of the specimens is shown in Fig. 4c. The surface energy of PEKK, PT20 and PT40 was 32.20 ± 1.10 mJ/m^2, 46.70 ± 1.30 mJ/m^2 and 53.80 ± 1.40 mJ/m^2, respectively.

Fig. 4d reveals the protein adsorption on the specimens. The BSA adsorption amount on PEKK, PT20 and PT40 was 3.21 ± 0.12 μg/cm^2, 8.54 ± 0.33 μg/cm^2 and 15.59 ± 0.53 μg/cm^2. In addition, the Fn adsorption amount on PEKK, PT20 and PT40 was 2.28 ± 0.13 μg/cm^2, 5.81 ± 0.29 μg/cm^2 and 9.98 ± 0.42 μg/cm^2, respectively.

3.4. Cell morphology, adhesion and proliferation, ALP activity

As shown in Fig. 5 (a, b, e, f, i, j), the cytoskeleton (green) and cell nuclei (blue) in MC3T3-E1 cells on the specimens were stained with FITC-Phalloidin and DAPI, respectively. At 1 day after culturing, the cells on PT20 and PT40 exhibited some filopodia while the cells on PEKK exhibited a spherical shape with no obvious filopodia. Moreover, more filopodia and lamel-lipodia of the cells increased with time. At 3 days after culturing, more filopodia and lamel-lipodia of the cells were found on PT40 than PT20, and PT20 than PEKK. The cells on PT40 almost covered the sample surface while cells on PEKK showed a lower density.

Fig. 5 (c, d, g, h, k, l) reveals the SEM images of the cells on the specimens at different time after culturing. At 1 day after culturing, the cells on PT20 and PT40 exhibited some filopodia while the cells on PEKK exhibited a spherical shape with no obvious filopodia. At 3 days after culturing, more filopodia and lamel-lipodia of the cells were found on PT40 than PT20, and PT20 than PEKK.

CCK-8 was used to investigate the adhesion and proliferation of MC3T3-E1 cells on the specimens at different time after culturing. As shown in Fig. 6a, it was found that the cell adhesion for both PT20 and PT40 increased with time while no obvious increase for PEKK. Moreover, at 24 and 48 h after culturing, the cell adhesion for PT40 were

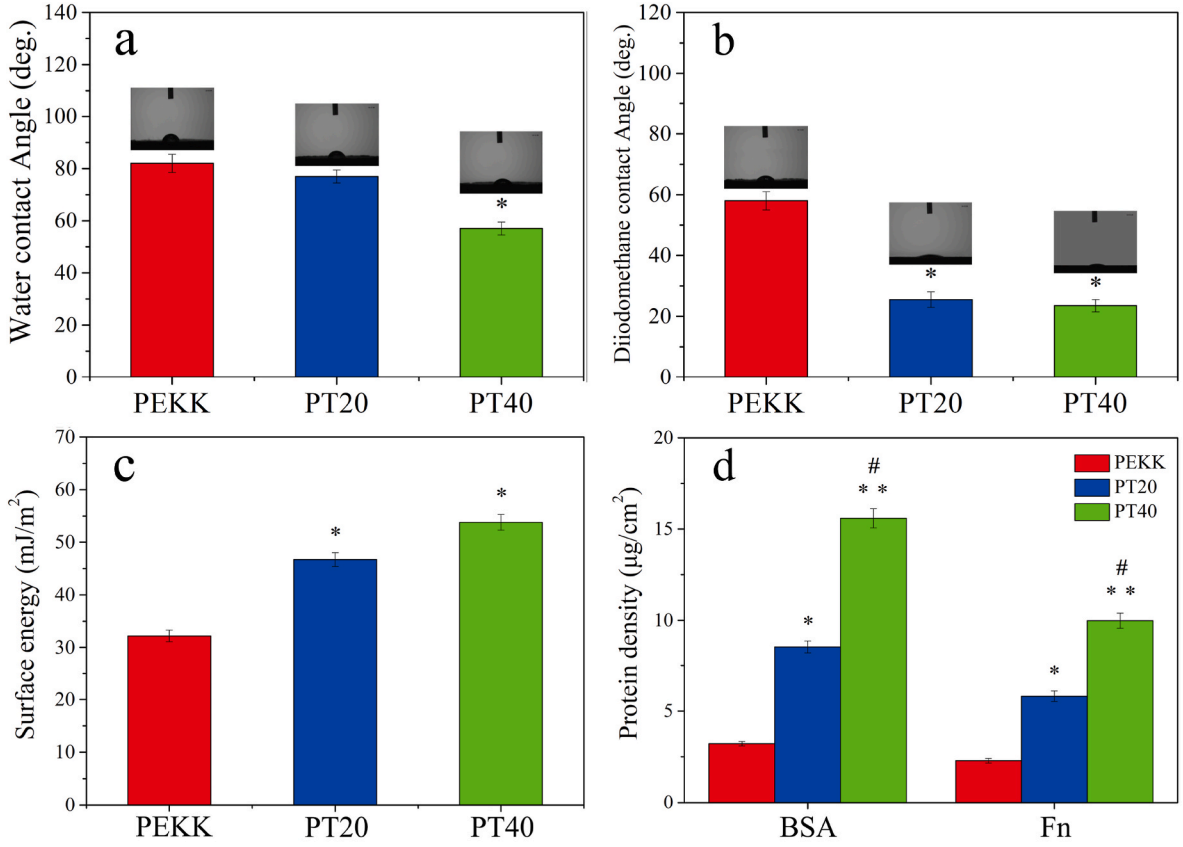

Fig. 4. Water contact angle (a) and diiodomethane contact angle (b) of PEKK, PT20 and PT40; Total surface energy (c) of PEKK, PT20 and PT40 by using Owens two-liquid method; Protein adsorption (d) on PEKK, PT20 and PT40 in 5 mg/mL BSA, 30 μg/mL Fn solutions, respectively. (* represents $p < 0.05$, ** represents $p < 0.01$, in comparison with PEKK; # represents $p < 0.05$, PT40 vs PT20).

higher than PT20, and PT20 were higher than PEKK.

Shown in Fig. 6b, the OD values of the cells for both PT20, and PT40 increased with time while no obvious increase for PEKK. In addition, at day 1, day 3, day 7, the OD values of cells on PT40 were higher than PT20, and PT20 were higher than PEKK.

The quantitative determination of ALP activity of MC3T3-E1 cells

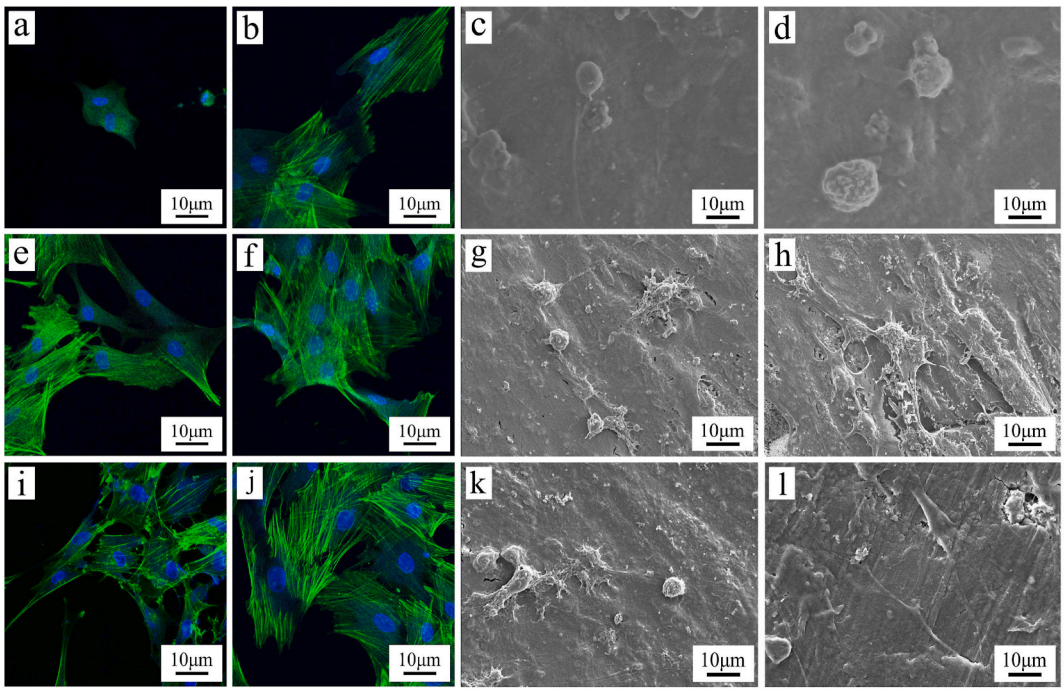

Fig. 5. CLSM photos of cytoskeletal morphology and spreading of MC3T3-E1 cells on PEKK (a, b), PT20 (e, f) and PT40 (i, j), and SEM images of cells on PEKK (c, d), PT20 (g, h) and PT40 (k, l) at 1 day (a, c, e, g, i, k) and 3 days (b, d, f, h, j, l) after culturing.

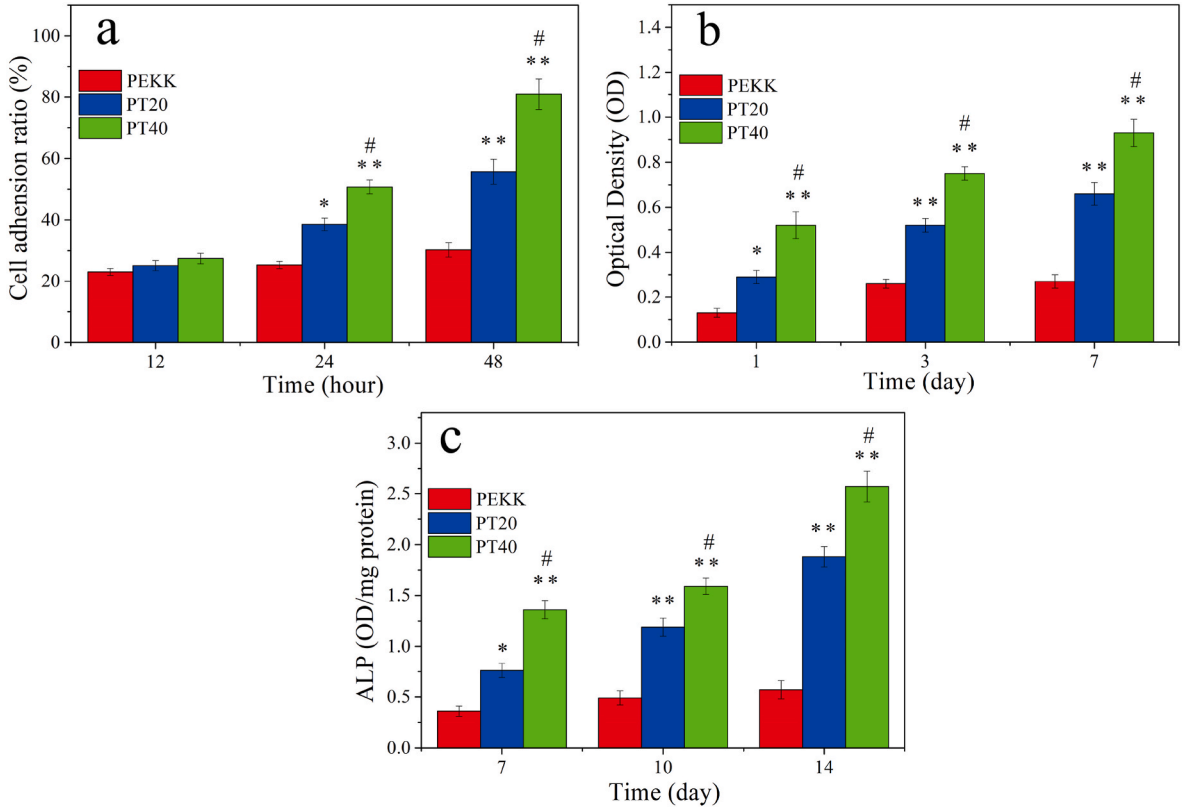

Fig. 6. Adhesion ratio (a), OD values (b) and ALP activity (c) of MC3T3-E1 cells on the specimens at different time after culturing (* represents $p < 0.05$, ** represents $p < 0.01$, compared with PEKK; # represents $p < 0.05$, PT40 vs PT20).

on the specimens at different time is shown in Fig. 6c. The ALP activity of the cells for both PT40 and PT20 increased with time but no obvious increase for PEKK. In addition, at day 7, 10 and 14, the ALP activity of the cells for PT40 was higher PT20, and PT20 was higher than PEKK.

3.5. Osteogenic related genes expressions

The expressions of osteogenesis genes including Runx2, ALP, OPN and OCN of the cells on PEKK, PT20 and PT40 were investigated by RT-PCR, and the results are shown in Fig. 7. The genes expressions for both PT40 and PT20 increased with time but no obvious increase for PEKK. At day 3, there were no obvious difference in the expression of Runx2, ALP, OPN and OCN for all specimens. At day 7 and 14, the expressions of Runx2, ALP, OPN, OCN for PT40 were higher than PT40, and PT20 were higher than PEKK.

3.6. Bone formation and osseointegration of implants in vivo

3.6.1. Micro-CT analysis

The 3D-reconstructed images of new bone tissues (NB) around the specimens from Micro-CT after implantation at different time are revealed in Fig. 8. The amounts of NB around PEKK, PT20 and PT40 increased with the implanted time. Moreover, at week 4 and 12 after implantation, the amounts of NB around the implants for PT40 were the highest while PEKK were the lowest.

The quantitative analysis of new bone formation around implants, including bone mineral density (BMD), bone volume/total volume (BV/TV), trabecular number (Tb.N) and trabecular thickness (Tb.Th) after implantation at different time are shown in Fig. 9. The BMD, BV/TV, Tb.N and Tb.Th for both PT40 and PT20 increased with time but no obvious increase for PEKK. At both week 4 and 12, the new bone formation for PT40 revealed the highest while PEKK was the lowest.

3.6.2. Histological, Bone-Implant Contact and push-out loads analysis

Fig. 10 is the histological images at different time after implantation. At week 4 and 12 after implantation, a larger amount of NB was seen for both PT20 and PT40 while a few NB was seen for PEKK, and the NB for PT40 was the highest. In addition, obvious gap at the interface between the NB and PEKK was found while the NB was in close contact with PT40 without gap at week 12, indicating good osseointegration.

Fig. 11a reveals the quantitative analysis of bone implant contact (BIC) at different time after implanted *in vivo*. The BIC of both PT20 and PT40 significantly increased from week 4–12 but there is no significant increase of PEKK. In addition, at both week 4 and 12, the BIC for both PT20 and PT40 were significantly higher than PEKK, and PT40 exhibited the highest.

Fig. 11b reveals the push out loads of the implants at different time after implantation. The push out loads for both PT20 and PT40 increased from week 4–12 but there was slightly increase for PEKK. Moreover, at both week 4 and 12, the push out loads for both PT20 and PT40 were remarkably higher than PEKK, and PT40 exhibited the highest.

4. Discussions

As an implant for orthopedic application, it should possess excellent biocompatibility and bioactivity, which act as a support substrate for cell adhesion, proliferation, osteogenic differentiation, and extracellular matrix deposition with consequent bone on-growth until the new bone tissues are fully combined with the implants to achieve osteointegration [28]. Therefore, the rapid new bone formation and osteointegration are essential for the initial and long-term stability of implants. Although PEKK has been widely applied as implants in orthopedics, it is bioinert material that might hardly promote new bone formation and osteointegration [29]. In this study, to design an

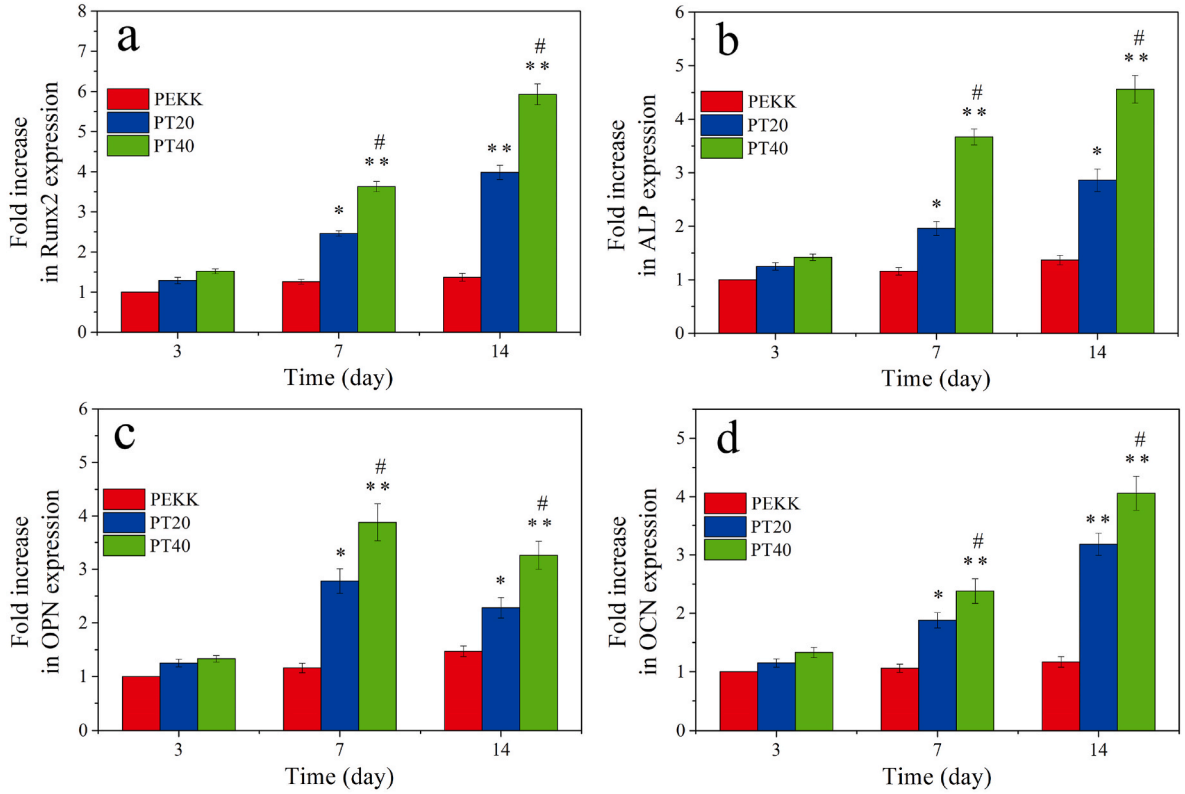

Fig. 7. Expressions of osteogenic genes of Runx2 (a), ALP (b), OPN (c) and OCN (d) of MC3T3-E1 cells on the specimens at different time after culturing (* represents $p < 0.05$, ** represents $p < 0.01$, compared with PEKK; # represents $p < 0.05$, PT40 vs PT20).

implantable material with high bioactivity for rapid new bone formation and osteointegration, PEKK/Ta composite were fabricated by incorporation of Ta microparticles (size of around 1 μm) into PEKK.

Surface roughness of implantable materials is one of the vital factors that influence the behaviors and functions of cells [30]. Our results showed that the PEKK/Ta composites with Ta particles of 40 v% (PT40) and 20 v% (PT20) content exhibited rougher surface compared to PEKK with a smooth surface. Moreover, Ta microparticles were found to disperse on the surface of the composites, and more Ta particles were found on PT40 than PT20. For the surface roughness, PT40 (5.30 μm) and PT20 (4.49 μm) were higher than PEKK (2.91 μm). Compared with PEKK, the significant increases of surface roughness of both PT40 and

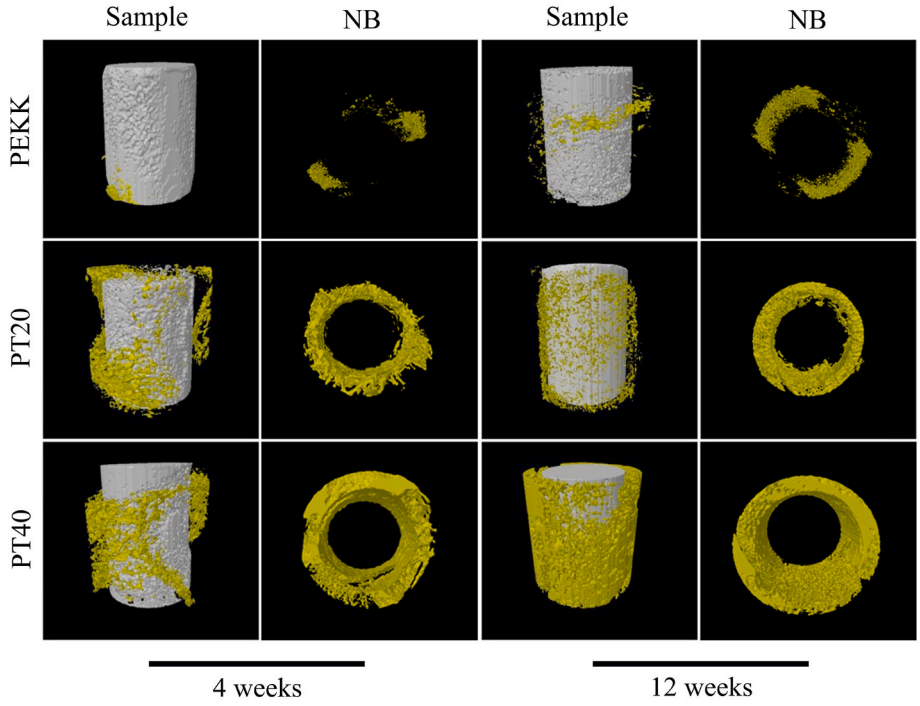

Fig. 8. 3D reconstructed images of new bone formation (NB) around the implants (PEKK, PT20, PT40) from Micro-CT at week 4 and 12 after implantation.

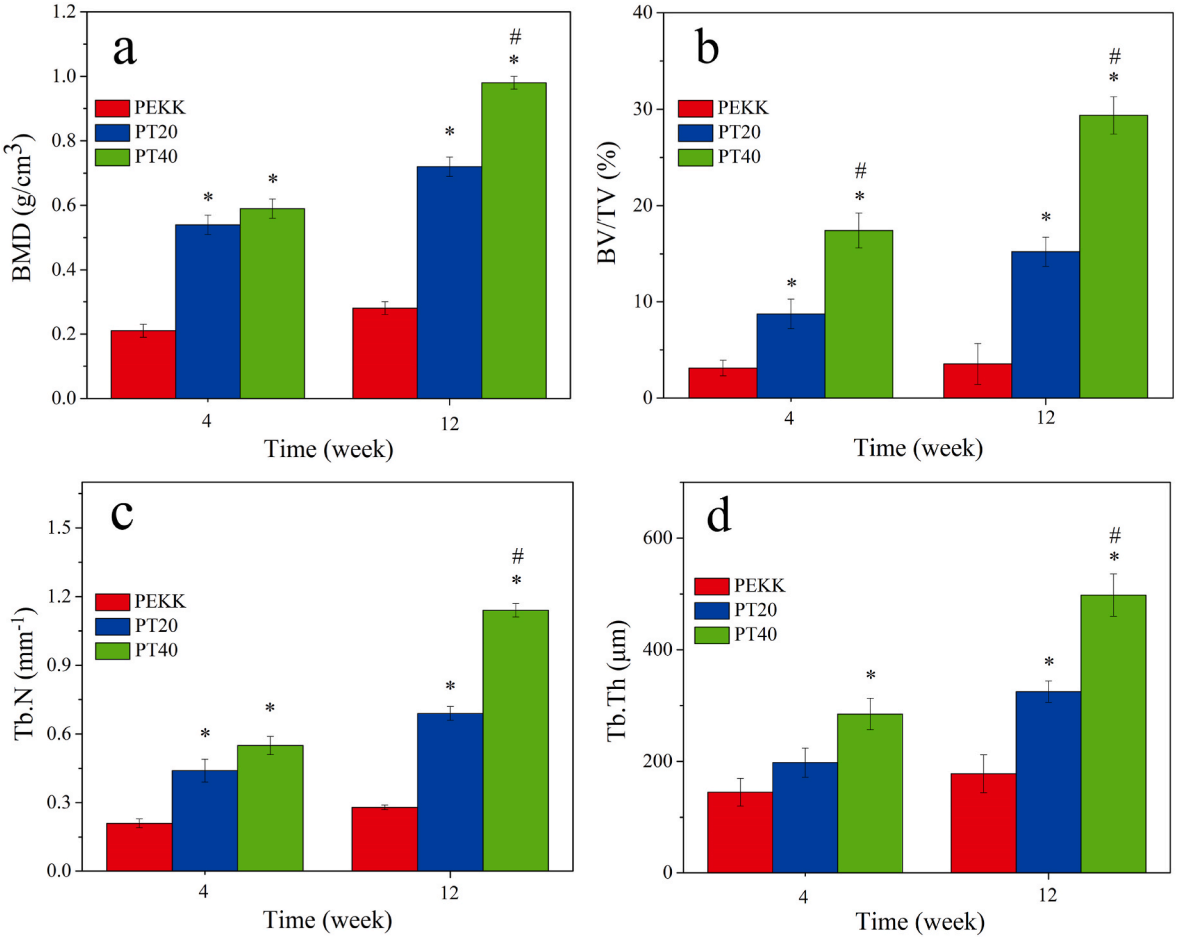

Fig. 9. Quantitative analysis of new bone formation around implants, including bone mineral density (BMD), bone volume/total volume (BV/TV), trabecular number (Tb.N) and trabecular thickness (Tb.Th) determination from Micro-CT at week 4 and 12 after implantation (* represents $p < 0.05$, compared with PEKK; # represents $p < 0.05$, PT40 vs PT20).

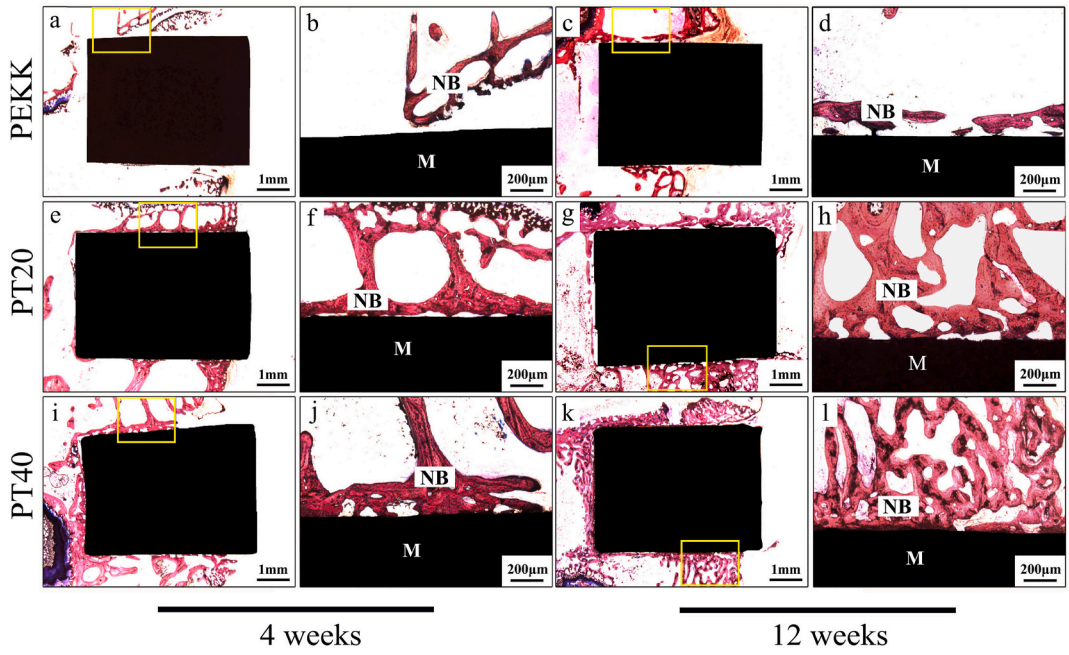

Fig. 10. Histological images under different magnifications of PEKK (a, b, c, d), PT20 (e, f, g, h) and PT40 (i, j, k, l) at week 4 (a, b, e, f, i. j) and 12 (c, d, g, h, k, l) after implanted *in vivo*, in which images (b, d, f, h, j and l) are the enlarged images of yellow small frame in images (a, c, e, g, i and k), NB represents new bone, and M represents materials. (For interpretation of the references to colour in this figure legend, the reader is referred to the Web version of this article.)

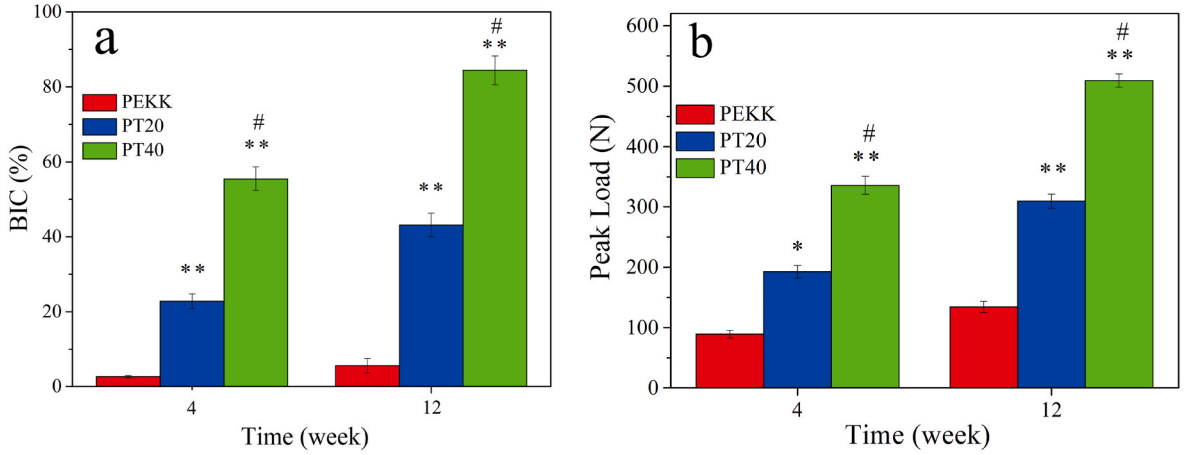

Fig. 11. Quantitative analysis of bone implant contact (a) and push-out loads (b) of implants (PEKK, PT20, PT40) at 4 and 12 weeks after implantation *in vivo* (* represents $p < 0.05$, ** represents $p < 0.01$, in comparison with PEKK; # represents $p < 0.05$, PT40 vs PT20).

PT20 were due to the presence of Ta microparticles on their surface. Moreover, PT40 with the higher Ta content exhibited the higher roughness than PT20. Generally, rough surface facilitates cell adhesion and spreading because the roughened surface possesses a higher surface area, which can offer more binding sites of adhesive protein that is an essential prerequisite for cell adhesion [31].

Hydrophilic surface of implantable materials facilitates the initial blood contact, promoting cell attachment, stimulating cell proliferation and differentiation, and accelerating osseointegration [32]. In this study, the surface hydrophilicity of both PT20 and PT40 containing Ta microparticles was obviously higher than PEKK. PEKK is polymer with hydrophobic surface while Ta is metal material with hydrophilic surface [33]. Therefore, compared with PT20 and PEKK, PT40 exhibited higher hydrophilicity due to more Ta particles distributed on its surface. In comparison with the hydrophobic surface, hydrophilic material surface is better for cell attachment, spreading, and cytoskeletal organization, because the improvement of surface hydrophilicity makes the surface more favorable for protein adsorption [34]. Implantable materials with high surface energy are bioactive, which will adsorb proteins in biological micro-environment, and the adsorbed protein will further attract surrounding cells and accelerate new bone formation [35]. In this study, the surface energy of both PT40 (53.80 mJ/m^2) and PT20 (46.70 mJ/m^2) containing Ta microparticles was obvious higher than PEKK (32.20 mJ/m^2). Furthermore, compared with PT20, PT40 exhibited higher surface energy due to more Ta particles with high surface energy distributed on its surface. Therefore, PT40 with high surface energy might provide the required micro-environment for starting the desired responses with the osteogenic cells/bone tissues.

It is commonly known that some behaviors and functions of cells are related to the performances of proteins absorption on implantable materials [36]. These adsorbed proteins could serve as ligands to bind to cell membrane protein receptors (integrins) leading to cell/materials adhesion [36]. For example, Fn plays a vital role in the initial cell adhesion and spreading on materials, because it can specially bind to integrins on cell membranes [37]. In this study, the proteins adsorption of PT40 (BSA: 15.59 $\mu g/cm^2$, Fn: 9.98 $\mu g/cm^2$) exhibited the highest in comparison with PT20 (BSA: 8.54 $\mu g/cm^2$, Fn: 5.81 $\mu g/cm^2$) and PEKK (BSA: 3.21 $\mu g/cm^2$, Fn: 2.28 $\mu g/cm^2$). Clearly, the significant increase of proteins adsorption of PT40 was due to more Ta particles distributed on its surface, which improved the surface performances of hydrophilicity, surface energy and roughness.

The interaction of cells with the implant surface mainly depends on the surface topographical features as well as chemical composition [38]. Adhesion of osteogenic cells to the substrate is crucial for the cell proliferation as well as differentiation on the implant [39]. In the study, for the adhesion of MC3T3-E1 cells on the specimens, both PT20 and PT40 containing Ta particles exhibited obviously higher cell adhesion than PEKK. Moreover, PT40 with higher Ta content showed higher cell adhesion than PT20. Efficacious adhesion is essential for the subsequent proliferation as well as differentiation of the cells [40]. In the study, for the proliferation of MC3T3-E1 cells on the specimens, both PT20 and PT40 containing Ta particles exhibited obviously higher cell proliferation than PEKK. Moreover, PT40 with higher Ta content showed higher cell proliferation than PT20. The attachment and proliferation of cells intensively pertain to the surface characteristics of the implant such as chemical composition, roughness, hydrophilicity and surface energy as well as proteins adsorptions [41]. Therefore, compared with PT20 and PEKK, the improvement of cell adhesion and proliferation on PT40 was because of more Ta particles distributed on its surface, which had improved surface performances that remarkably promoted cell responses.

Among the main osteogenic marks, during the early period of osteogenesis, the improvement of ALP activity is a vital event occurring [42]. In the study, for the ALP activity of cells on the specimens, both PT20 and PT40 containing Ta particles revealed higher ALP activity than PEKK. Moreover, compared with PT20, PT40 with higher Ta content showed higher ALP activity. In addition, the Runx2, ALP, OPN and OCN are the most important osteogenesis related genes expressed by osteoblasts [43]. In the study, the results showed that at day 7 and day 14, the expression of Runx2, ALP, OPN, OCN on PT20 and PT40 were significantly higher than PEKK, and PT40 exhibited the highest expressions of osteogenesis genes among all specimens. Clearly, compared with PT20 and PEKK, PT40 with high Ta content enhanced the expressions of osteogenesis genes. Therefore, it could be suggested that PT40 with high Ta content had improved surface properties, which remarkably enhanced the osteogenic differentiation of cells.

As for successful orthopedic implantation, the new bone formation and osseointegration can be accomplished through providing optimal bone remodeling at the interface of bone tissues and implantable materials [44]. The *in vivo* investigations were further conducted to determine the effects of Ta content on new bone formation and osseointegration. The results of 3D reconstructed images as well as quantitative analysis of new bone formation (NB) around the implants from Micro-CT showed that the amounts of NB around the implants for PT20 and PT40 were significantly higher than PEKK at week 4 and 12 after implantation, and PT40 exhibited the highest among all specimens. Compared with PT20 and PEKK, PT40 with high Ta content remarkably promoted new bone formation. Moreover, the osseointegration of implants with the host bone tissue was determined by the push out loads. It was found that the push out loads for both PT20 and PT40 were remarkably higher than PEKK, and PT40 exhibited the highest, indicating the best osseointegration.

As an endosseous implant, it is crucial to achieve a direct contact

with the bone tissues, and thus to guarantee the osseointegration quality of the implants for its long-term success [8]. In this study, the histological images revealed that the amount of NB formation for PT40 and PT20 were higher than PEKK, and PT40 exhibited the highest bone formation among all specimens. Moreover, a relatively gap zone was found between the NB and PEKK surface while the NB was closely contact with PT40 surface, indicating good osseointegration. Clearly, compared with PT20 and PEKK, PT40 with high Ta content significantly promote bone formation and osseointegration. Osseointegration is a biological-chemical process that achieves the stable anchorage of the implants obtained by bone to implant contact (BIC) [45]. In this study, the quantitative analysis showed that the BIC of both PT20 and PT40 significantly increased from week 4–12 but no significant increase of PEKK. Moreover, at both week 4 and 12, the BIC for both PT20 and PT40 were significantly higher than PEKK, and PT40 exhibited the highest, indicating good osseointegration.

The surface performances (chemical composition, morphology, hydrophilicity and surface energy, roughness, etc.) of the implantable materials affect not only the cell responses but also the osteogenesis and osseointegration [46]. Some studies have shown that a rougher surface with high hydrophilicity as well as surface energy commonly promoted fibrin clot attachment, cell adhesion, proliferation and osteogenic differentiation, and thus enhanced the bone formation and osseointegration [47]. In the present study, in comparison with PEKK, incorporation of Ta microparticles into PEKK created implantable composites (including PT20 and PT40) with improved surface performances (e.g., hydrophilicity, surface energy, roughness and proteins adsorption), which played key roles in stimulating the responses (e.g., adhesion, proliferation and differentiation) of MC3T3-E1 cells *in vitro*, and thus promoted bone formation and osseointegration *in vivo*. Clearly, compared with PEKK and PT20, PT40 containing high Ta content exhibited optimized surface performances. Furthermore, PT40 with high Ta content had improved mechanical performances (e.g., compressive strength and modulus of elasticity), which is close to the cortical bone of human [26,27]. In short, PT40 with excellent biocompatibility, improved mechanical performances and bioactivity stimulated cell responses, and promoted osseointegration, which might have tremendous potential for bear-loading bone substitute.

5. Conclusions

In the present study, implantable biocomposites of PEKK/Ta were prepared by blending PEKK with Ta microparticles. The surface hydrophilicity, surface energy, roughness and proteins adsorption of PT40 containing high Ta particles content were significantly higher than PT20 and PEKK. Compared with PT20 and PEKK, the mechanical performances of PT40 were enhanced, which were close to the cortical bone of human. In addition, PT40 remarkably stimulated the responses (adhesion, proliferation and osteogenic differentiation) of MC3T3-E1 cells *in vitro*. Furthermore, PT40 obviously enhanced new bone formation and osseointegration *in vivo*. In brief, incorporation of Ta microparticles into PEKK created implantable composites with improved surface performances, which significantly stimulated cell responses and promoted osseointegration both *in vitro* and *in vivo*. PT40 with excellent biocompatibility and bioactivity could have huge potential for bear-loading bone substitute.

CRediT authorship contribution statement

Xinglong Hu: Investigation, Conceptualization, Methodology, Formal analysis, Writing - original draft. **Shiqi Mei:** Methodology, Formal analysis, Data curation. **Fan Wang:** Investigation, Data curation. **Jun Qian:** Investigation, Formal analysis. **Dong Xie:** Methodology, Validation. **Jun Zhao:** Methodology, Resources, Data curation, Validation. **Lili Yang:** Conceptualization, Methodology, Formal analysis, Writing - review & editing. **Zhaoying Wu:** Visualization, Validation. **Jie Wei:** Supervision, Writing - review & editing, Project administration.

CRediT authorship contribution statement

Xinglong Hu: Investigation, Conceptualization, Methodology, Formal analysis, Writing - original draft. **Shiqi Mei:** Methodology, Formal analysis, Data curation. **Fan Wang:** Investigation, Data curation. **Jun Qian:** Investigation, Formal analysis. **Dong Xie:** Methodology, Validation. **Jun Zhao:** Methodology, Resources, Data curation, Validation. **Lili Yang:** Conceptualization, Methodology, Formal analysis, Writing - review & editing. **Zhaoying Wu:** Visualization, Validation. **Jie Wei:** Supervision, Writing - review & editing, Project administration.

Declaration of competing interest

The authors declare no conflict of interest.

Acknowledgements

The grants were from Key Medical Program of Science and Technology Development of Shanghai (17441902000 and 19441906100), the National Natural Science Foundation of China (81771990 and 81801845) and Shenzhen Fundamental Research Program (JCYJ20190807160811355).

References

[1] Q. Han, C. Wang, H. Chen, X. Zhao, J. Wang, Porous tantalum and titanium in orthopedics: a review, ACS Biomater. Sci. Eng. 5 (2019) 5798–5824.
[2] C. Yang, J. Li, C. Zhu, Q. Zhang, J. Yu, J. Wang, Q. Wang, J. Tang, H. Zhou, H. Shen, Advanced antibacterial activity of biocompatible tantalum nanofilm via enhanced local innate immunity, Acta Biomater. 89 (2019) 403–418.
[3] C. Hwang, S. Park, I. Kang, H. Kim, C. Han, Tantalum-coated polylactic acid fibrous membranes for guided bone regeneration, Mater. Sci. Eng. C Mater. Biol. Appl 115 (2020) 111112.
[4] E. Gee, R. Jordan, J. Hunt, A. Saithna, Current evidence and future directions for research into the use of tantalum in soft tissue re-attachment surgery, J. Math. Chem. B 4 (2016) 1020–1034.
[5] W. Huo, L. Zhao, S. Yu, Z. Yu, P. Zhang, Y. Zhang, Significantly enhanced osteoblast response to nano-grained pure tantalum, Sci. Rep. 7 (2017) 40868.
[6] C. Kang, L. Wei, B. Song, L. Chen, J. Liu, B. Deng, X. Pan, L. Shao, Involvement of autophagy in tantalum nanoparticle-induced osteoblast proliferation, Int. J. Nanomed. 12 (2017) 4323–4333.
[7] J. Ninomiya, J. Struve, J. Krolikowski, M. Hawkins, D. Weihrauch, Porous ongrowth surfaces alter osteoblast maturation and mineralization, J. Biomed. Mater. Res. 103 (2015) 276–281.
[8] C. Park, Y. Seong, I. Kang, E. Song, H. Lee, J. Kim, H. Jung, H. Kim, T. Jang, Enhanced osseointegration ability of poly(lactic acid) via tantalum sputtering-based plasma immersion ion implantation, ACS Appl. Mater. Interfaces 11 (2019) 10492–10504.
[9] S. Asadullah, H. Wu, S. Mei, D. Wang, Y. Pan, D. Wang, J. Zhao, J. Wei, Preparation, characterization, in vitro bioactivity and rBMSCs responses to tantalum pentoxide/polyimide biocomposites for dental and orthopedic implants, Compos. B Eng. 177 (2019) 107433.
[10] F. Wang, C. Li, S. Zhang, H. Liu, Tantalum coated on titanium dioxide nanotubes by plasma spraying enhances cytocompatibility for dental implants, Surf. Coating. Technol. 382 (2020) 125161.
[11] W. Liu, H. Wang, C. Liu, J. Wang, X. Cheng, C. Liu, L. Qiao, S. Zhang, X. Jian, RhBMP-2 immobilized on poly(phthalazinone ether nitrile ketone) via chemical and physical modification for promoting in vitro osteogenic differentiation, Colloids Surf. B Biointerfaces 194 (2020) 111173.
[12] G. Cai, H. Wang, Y. Jung, Z. Xu, J. Zhang, J. He, D. Wang, J. Shin, R. Kaewmanee, S. Nabanita, J. Wei, Hierarchically porous surface of PEEK/nMCS composite created by femtosecond laser and incorporation of resveratrol exhibiting antibacterial performances and osteogenic activity in vitro, Compos. B Eng. 186 (2020) 107802.
[13] E. Long, M. Buluk, M. Gallagher, J. Schneider, J. Brown, Human mesenchymal stem cell morphology, migration, and differentiation on micro and nano-textured titanium, Bioact. Mater 4 (2019) 249–255.
[14] S. Ouyang, Q. Huang, Y. Liu, Z. Ouyang, L. Liang, Powder metallurgical Ti-Mg metal-metal composites facilitate osteoconduction and osseointegration for orthopedic application, Bioact. Mater 4 (2019) 37–42.
[15] A. Gao, Q. Liao, L. Xie, G. Wang, W. Zhang, Y. Wu, P. Li, M. Guan, H. Pan, L. Tong, P. Chu, H. Wang, Tuning the surface immunomodulatory functions of polyetheretherketone for enhanced osseointegration, Biomaterials 230 (2020) 119642.

[16] J. Lin, I. Mohamed, P. Lin, H. Shirahama, U. Milbreta, J. Sieow, Y. Peng, M. Bugiani, S. Wong, H. Levinson, Modulating macrophage phenotype by sustained MicroRNA delivery improves host-implant integration, Adv. Healthc. Mater 9 (2019) 1901257.
[17] T. Wan, Z. Jiao, M. Guo, Z. Wang, Y. Wan, K. Lin, Q. Liu, P. Zhang, Gaseous sulfur trioxide induced controllable sulfonation promoting biomineralization and osseointegration of polyetheretherketone implants, Bioact. Mater 5 (2020) 1004–1017.
[18] R. Ma, Q. Li, L. Wang, X. Zhang, L. Fang, Z. Luo, B. Xue, L. Ma, Mechanical properties and in vivo study of modified-hydroxyapatite/polyetheretherketone biocomposites, Mater. Sci. Eng. C Mater. Biol. Appl 73 (2017) 429–439.
[19] H. Wu, T. Liu, Z. Xu, J. Qian, X. Shen, Y. Li, Y. Pan, D. Wang, K. Zheng, A. Boccaccini, J. Wei, Enhanced bacteriostatic activity, osteogenesis and osseointegration of silicon nitride/polyetherketoneketone composites with femtosecond laser induced micro/nano structural surface, Appl. Mater. Today 18 (2020) 100523.
[20] R. Ma, Z. Yu, S. Tang, Y. Pan, J. Wei, T. Tang, Osseointegration of nanohydroxyapatite- or nanocalcium silicate-incorporated polyetheretherketone bioactive composites in vivo, Int. J. Nanomed. 11 (2016) 6023–6033.
[21] H. Zhu, X. Ji, H. Guan, L. Zhao, L. Zhao, C. Liu, C. Cai, W. Li, T. Tao, J. Reseland, H. Haugen, J. Xiao, Tantalum nanoparticles reinforced polyetheretherketone shows enhanced bone formation, Mater. Sci. Eng. C Mater. Biol. Appl 101 (2019) 232–242.
[22] T. Lu, J. Wen, S. Qian, H. Cao, C. Ning, X. Pan, X. Jiang, X. Liu, P. Chu, Enhanced osteointegration on tantalum-implanted polyetheretherketone surface with bone-like elastic modulus, Biomaterials 51 (2015) 173–183.
[23] B. Yuan, Q. Cheng, R. Zhao, X. Zhu, X. Yang, X. Yang, K. Zhang, Y. Song, X. Zhang, Comparison of osteointegration property between PEKK and PEEK: effects of surface structure and chemistry, Biomaterials 170 (2018) 116–126.
[24] B. Yuan, Y. Chen, H. Lin, Y. Song, X. Yang, H. Tang, E. Xie, T. Hsu, X. Yang, X. Zhu, K. Zhang, X. Zhang, Processing and properties of bioactive surface-porous PEKK, ACS Biomater. Sci. Eng. 2 (2016) 977–986.
[25] Z. Tan, J. Sun, C. Wu, J. Qiu, C. Liu, Phosphorus-containing polymers from THPS. IV: Synthesis and properties of phosphorus-containing polybenzoxazines as a green route for recycling toxic phosphine (PH3) tail gas, J. Hazard Mater. 322 (2017) 540–550.
[26] X. Dong, R. Acuna, Q. Luo, X. Wang, Orientation dependence of progressive post-yield behavior of human cortical bone in compression, J. Biomech. 45 (2012) 2829–2834.
[27] D. Singh, A. Rana, S. Jhajhria, B. Garg, P. Pandey, D. Kalyanasundaram, Experimental assessment of biomechanical properties in human male elbow bone subjected to bending and compression loads, J. Appl. Biomater. Funct. Mater. 17 (2019) 2280800018793816.
[28] P. Gao, B. Fan, X. Yu, W. Liu, J. Wu, L. Shi, D. Yang, L. Tan, P. Wan, Y. Hao, S. Li, W. Hou, K. Yang, X. Li, Z. Guo, Biofunctional magnesium coated Ti6Al4V scaffold enhances osteogenesis and angiogenesis in vitro and in vivo for orthopedic application, Bioact. Mater 5 (2020) 680–693.
[29] J. Khoury, I. Selezneva, S. Pestov, V. Tarassov, A. Ermakov, A. Mikheev, M. Lazov, S. Kirkpatrick, D. Shashkov, A. Smolkov, Surface bioactivation of PEEK by neutral atom beam technology, Bioact. Mater 4 (2019) 132–141.
[30] K. Li, Y. Xue, T. Yan, L. Zhang, Y. Han, Si substituted hydroxyapatite nanorods on Ti for percutaneous implants, Bioact. Mater 5 (2020) 116–123.
[31] F. Yin, R. Xu, S. Hu, K. Zhao, S. Zhao, S. Yang, S. Kuang, Q. Li, Q. Han, Enhanced mechanical and biological performance of an extremely fine nanograined 316L stainless steel cell-substrate interface fabricated by ultrasonic shot peening, ACS Biomater. Sci. Eng. 4 (2018) 1609–1621.
[32] L. Fialho, S. Carvalho, Surface engineering of nanostructured Ta surface with incorporation of osteoconductive elements by anodization, Appl. Surf. Sci. 495 (2019) 143573.
[33] H. Ghorbani, A. Abdollah-Zadeh, F. Bagheri, A. Poladi, Improving the bio-corrosion behavior of AISI316L stainless steel through deposition of Ta-based thin films using PACVD, Appl. Surf. Sci. 456 (2018) 398–402.
[34] D. Lin, L. Fuh, W. Chen, Nano-morphology, crystallinity and surface potential of anatase on micro-arc oxidized titanium affect its protein adsorption, cell proliferation and cell differentiation, Mater. Sci. Eng. C Mater. Biol. Appl 107 (2020) 110204.
[35] M. Chen, Y. Zhang, W. Zhang, J. Li, Polyhedral oligomeric silsesquioxane-incorporated gelatin hydrogel promotes angiogenesis during vascularized bone regeneration, ACS Appl. Mater. Interfaces 12 (2020) 22410–22425.
[36] J. Sefkow-Werner, P. Machillot, A. Sales, E. Castro-Ramirez, M. Degardin, D. Boturyn, E.A. Cavalcanti-Adam, C. Albiges-Rizo, C. Picart, E. Migliorini, Heparan sulfate co-immobilized with cRGD ligands and BMP2 on biomimetic platforms promotes BMP2-mediated osteogenic differentiation, Acta Biomater. 114 (2020) 90–103.
[37] S. Wu, X. Liu, C. Gao, Role of adsorbed proteins on hydroxyapatite-coated titanium in osteoblast adhesion and osteogenic differentiation, Sci. Bull. 60 (2015) 691–700.
[38] R. An, P. Fan, M. Zhou, Y. Wang, S. Goel, X. Zhou, W. Li, J. Wang, Nanolamellar tantalum interfaces in the osteoblast adhesion, Langmuir 35 (2019) 2480–2489.
[39] J. Zhang, J. Liu, C. Wang, F. Chen, X. Wang, K. Lin, A comparative study of the osteogenic performance between the hierarchical micro/submicro-textured 3D-printed Ti6Al4V surface and the SLA surface, Bioact. Mater 5 (2020) 9–16.
[40] M. Li, A. Zhang, J. Li, J. Zhou, Y. Zheng, C. Zhang, D. Xia, H. Mao, J. Zhao, Osteoblast/fibroblast coculture derived bioactive ECM with unique matrisome profile facilitates bone regeneration, Bioact. Mater 5 (2020) 938–948.
[41] K. Liu, H. Zhang, M. Lu, L. Liu, Y. Yan, Z. Chu, Y. Ge, T. Wang, C. Tang, Enhanced bioactive and osteogenic activities of titanium by modification with phytic acid and calcium hydroxide, Appl. Surf. Sci. 478 (2019) 162–175.
[42] S. Sayed, O. Faruq, M. Hossain, S. Im, Y. Kim, B. Lee, Thermal cycling effect on osteogenic differentiation of MC3T3-E1 cells loaded on 3D-porous Biphasic Calcium Phosphate (BCP) scaffolds for early osteogenesis, Mater. Sci. Eng. C Mater. Biol. Appl 105 (2019) 110027.
[43] Z. Tang, T. Xu, Y. Li, W. Fei, G. Yang, Y. Hong, Inhibition of CRY2 by STAT3/miRNA-7-5p promotes osteoblast differentiation through upregulation of CLOCK/BMAL1/P300 expression, Mol. Ther. Nucleic Acids 19 (2020) 865–876.
[44] P. Xiu, Z. Jia, J. Lv, C. Yin, Y. Cheng, K. Zhang, C. Song, H. Leng, Y. Zheng, H. Cai, Z. Liu, Tailored surface treatment of 3D printed porous Ti6Al4V by microarc oxidation for enhanced osseointegration via optimized bone in-growth patterns and interlocked bone/implant interface, ACS Appl. Mater. Interfaces 8 (2016) 17964–17975.
[45] S. Barak, M. Neuman, G. Iezzi, A. Piattelli, V. Perrotti, Y. Gabet, A new device for improving dental implants anchorage: a histological and micro-computed tomography study in the rabbit, Clin. Oral Implants Res. 27 (2016) 935–942.
[46] W. Chrzanowski, J. Lee, A. Kondyurin, M. Lord, J. Jang, H. Kim, M. Bilek, Nano-Biochemical braille for cells: the regulation of stem cell responses using Bi-functional surfaces, Adv. Funct. Mater. 25 (2015) 193–205.
[47] J. Zhang, W. Zhou, H. Wang, K. Lin, F. Chen, 3D-printed surface promoting osteogenic differentiation and angiogenetic factor expression of BMSCs on Ti6Al4V implants and early osseointegration in vivo, J. Mater. Sci. Technol. 35 (2019) 336–343.